

See discussions, stats, and author profiles for this publication at: <https://www.researchgate.net/publication/5637411>

Direct Coprecipitation Route to Monodisperse Dual-Functionalized Magnetic Iron Oxide Nanocrystals Without Size Selection

ARTICLE *in* SMALL · FEBRUARY 2008

Impact Factor: 8.37 · DOI: 10.1002/sml.200700575 · Source: PubMed

CITATIONS

70

READS

77

5 AUTHORS, INCLUDING:



Zhen Li

University of Wollongong

107 PUBLICATIONS 3,017 CITATIONS

SEE PROFILE



Bien Tan

Huazhong University of Science and Techn...

112 PUBLICATIONS 2,232 CITATIONS

SEE PROFILE

DOI: 10.1002/sml.200700575

Direct Coprecipitation Route to Monodisperse Dual-Functionalized Magnetic Iron Oxide Nanocrystals Without Size Selection

Zhen Li, Bien Tan, Mathieu Allix, Andrew I. Cooper,* and Matthew J. Rosseinsky*

Water-soluble monodisperse superparamagnetic Fe₃O₄ nanocrystals decorated with two distinct functional groups are prepared in a single-step procedure by injecting iron precursors into a refluxing aqueous solution of a polymer ligand, trithiol-terminated poly(methacrylic acid) (PMAA-PTTM), bearing both carboxylate and thiol functionalities. The ratio of carboxylic acid groups in the polymer-protecting ligand to the iron precursors plays a key role in determining the particle size and particle size distribution. The surface functionalities of the ligands allow post-synthesis modification of the materials to produce water-soluble fluorescent magnetic nanocrystals.

Keywords:

- conjugation
- coprecipitation
- fluorescence
- magnetic nanomaterials


1. Introduction

Magnetic nanoparticles have shown potential for the ultrasensitive detection and separation of proteins and pathogens^[1] in biolabeling and imaging,^[2,3] and in clinical diagnosis and the treatment of diseases.^[4,5] Spinel structured AB₂O₄ ($A = \text{Fe}^{2+}$, Co^{2+} ; $B = \text{Fe}^{3+}$) ferrimagnetic insulating oxides are thus important synthetic targets. The size- and shape-controlled synthesis of water-soluble and biocompatible magnetic nanocrystals is key for such applications. For this reason, a range of synthetic techniques have been investigated such as coprecipitation, microemulsion processing, ultrasound irradiation, laser pyrolysis, thermal decomposition, and hydrothermal routes.^[6] These approaches may be divided into aqueous and nonaqueous routes. Aqueous approaches are attractive in terms of cost and sustainability;

there is, however, a generic challenge in directly obtaining water-soluble monodisperse magnetic nanoparticles without laborious size selection. This arises from the complexity of controlling the nucleation and growth processes and the complicated hydrolysis reactions of the iron precursors.^[7] Moreover, because most reactions are carried out at room temperature, the nanoparticles obtained often exhibit low crystallinity and low saturation magnetization. By contrast, thermal decomposition of organometallic iron precursors in organic solvents at high temperatures can yield very monodisperse and highly crystalline magnetic nanoparticles,^[8–10] since nucleation can be separated from growth and complex hydrolysis reactions can be avoided.^[8,10]

While the size and shape of magnetic nanoparticles can be controlled in nonaqueous systems, these products are generally only soluble in organic solvents; this limits their direct application in biomedical fields such as for in vivo applications. To prepare water-soluble magnetic nanoparticles, a second ligand-exchange step is generally required.^[1,3] In some cases, however, aggregation or flocculation of the nanoparticles occurs during the ligand-exchange reaction, especially for large particles.^[11] Recently, thermal decomposition methods have been modified to synthesize directly water-soluble magnetic nanoparticles using the strongly

[*] Dr. Z. Li, Dr. B. Tan, Dr. M. Allix, Prof. A. I. Cooper, Prof. M. J. Rosseinsky
Department of Chemistry, University of Liverpool
L69 7ZD (U.K.)
Fax: (+44) 151-794-3587
E-mail: aicooper@liv.ac.uk
mjrosseinsky@liv.ac.uk

 Supporting Information is available on the WWW under <http://www.small-journal.com> or from the author.

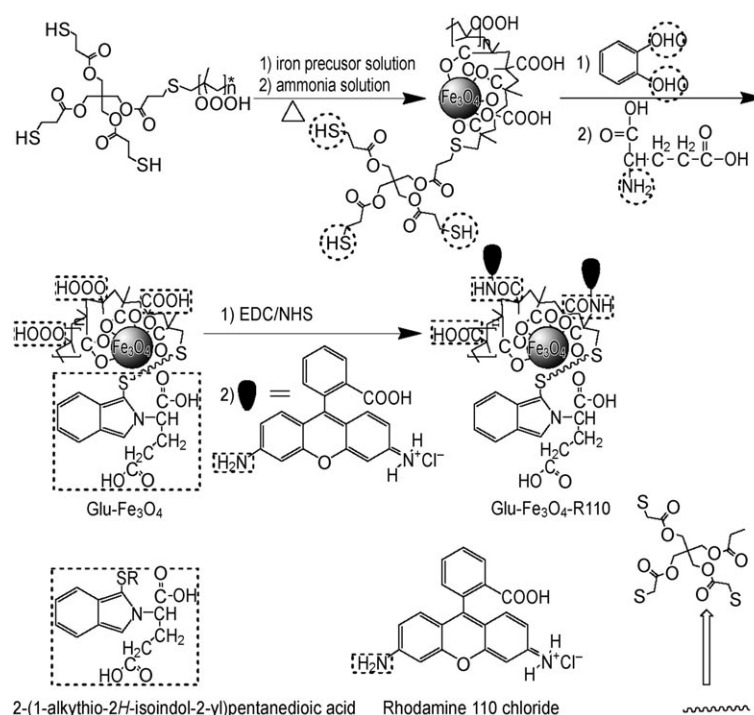
polar solvent 2-pyrrolidone as the reaction medium.^[12,13] Using similar strategies, functional biocompatible magnetic nanoparticles have been prepared in a one-pot reaction, which can then be used as magnetic resonance imaging (MRI) probes to detect cancer in vivo.^[14–16] These water-soluble magnetic nanoparticles show broader size distributions compared to those synthesized in non-polar solvents^[8–10] and have single functional groups.^[15,16] The development of a simple, low-cost, and environmentally friendly method to prepare high-quality magnetic nanoparticles with multifunctional surfaces (here “high-quality” refers to monodispersity, high crystallinity and high saturation magnetization) directly in water is thus an important goal.

A second target is to achieve facile surface functionalization of the magnetic nanoparticles in order to impart precise biological functions and to improve the site-specific target efficiency.^[17] Usually the reactive surfaces are generated by post-preparative surface modification,^[1–3] for example, multistep post-treatment of water-soluble particles has allowed the covalent bonding of HIV-tat peptide and other biomolecules to the surface of nanoparticles.^[2,17] For organic-soluble particles synthesized by thermal decomposition, multifunctional ligands are required as both phase-transfer agents to confer water solubility and as surface-coupling agents to provide reactive moieties for further attachment of bioligands.^[3]

In this paper, we report a single-step coprecipitation approach for preparing dual-functionalized monodisperse magnetic nanocrystals that are protected by a trithiol-terminated poly(methacrylic acid) ligand (PMAA-PTTM, number average molecular weight $M_n=4537$, polydispersity $M_w/M_n=1.21$).^[18,19] We then demonstrate that the two functional groups on the particle surfaces can be used to prepare fluorescent magnetic nanoparticles via a covalent conjugation reaction (Scheme 1), offering enhanced labeling capabilities compared to monofunctionalized surfaces.^[15,16]

2. Results and Discussion

Magnetic iron oxide nanoparticles were prepared by injecting an iron precursor solution and an ammonia solution into an aqueous polymer solution under reflux. For the direct preparation of 4.5-nm-diameter particles (see Experimental Section for details) the molar ratio between the poly-



Scheme 1. Preparation of polymer-functionalized Fe₃O₄ nanoparticles and subsequent conjugation reactions.

mer ligand carboxylic acid groups and FeCl₃·6H₂O is 3.4 and the solution concentration is 0.01 M. Figure 1a shows transmission electron microscopy (TEM) images of iron oxide nanoparticles obtained directly by one-shot injection without any subsequent size selection. The average particle size is 4.5 nm and the standard deviation is 0.4 nm as shown in Figure S1a (Supporting Information). The high-resolution

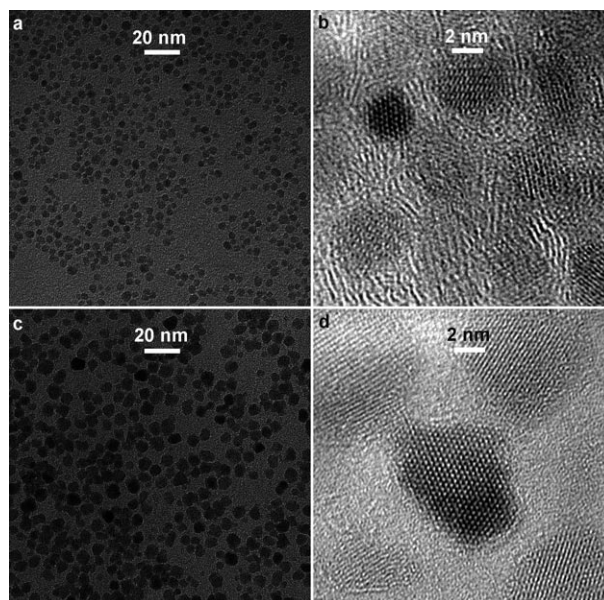


Figure 1. TEM and HRTEM images of a, b) 4.5-nm and c, d) 8.5-nm PMAA-PTTM protected Fe₃O₄ nanocrystals. The molar ratio between carboxylic acid groups and FeCl₃·6H₂O in both cases is 3.4.

TEM (HRTEM) presented in Figure 1b clearly shows that the product is highly crystalline despite the small particle size. During the preparation, it was important to inject the entire iron precursor in one shot because nanoparticles obtained from multishot injections showed a broader size distribution. Figure S2 shows the diameter and size distribution of nanoparticles prepared under the same conditions but with injection of the iron precursor solution in five shots with 10 minutes intervals between two successive injections. The particle size is 4.9 nm with a standard deviation of 1.4 nm.

Larger particles were prepared by a seed-mediated growth method.^[9,10] Figure 1c presents TEM images of the nanoparticles obtained by using the 4.5-nm particles shown in Figure 1a as seeds. The particle size distribution is shown in Figure S1b and the average particle size is 8.5 ± 0.8 nm. HRTEM again demonstrates the highly crystalline nature of the larger nanoparticles (Figure 1d).

These samples exhibit a narrow particle size distribution in comparison with magnetic nanoparticles obtained by multiple-shot injection and standard coprecipitation (Figure S2–S3).^[20] This is associated with the rapid injection of all of the iron precursors into the hot aqueous solution of the protecting polymer at one time. Rapid precursor injection has been used extensively to prepare monodisperse magnetic and other inorganic nanocrystals in organic solvents at high temperatures.^[8–10,21] For homogeneous preparations, the key to synthesizing monodisperse nanoparticles is to precisely control the nucleation process and the growth process by the supersaturation concentration of species.^[8,22] High supersaturation concentration favors nucleation while low supersaturation concentration favors growth.^[22]

Previously reported coprecipitation methods used dropwise addition with the aim of achieving a slow, continuous nucleation and growth process.^[23] It is hard to achieve this for Fe_3O_4 because of the difficulty of controlling the hydrolysis and condensation rate. Initially, the iron precursors are hydrolyzed under alkaline conditions and then condensed into iron oxide nuclei. With increased nuclei concentration, these nascent particles collide and grow into large-sized nuclei. The continuous dropwise addition of precursors yields fresh iron oxide nuclei of different size and reactivity. These nuclei form different-sized iron oxide nanoparticles and hence give rise to a broad size distribution. In addition, low temperatures decrease the reaction rate and the diffusion of active species, which also broadens the distribution.

In the present synthesis, the rapid injection of the iron precursors and ammonia solution into the refluxing poly-

mer solution caused rapid hydrolysis and condensation reactions. The injection of all of the iron precursors at one time yielded a higher concentration than dropwise addition, thus giving a high supersaturation concentration and a short burst of nucleation. The surface iron atoms of the nanoparticles were coordinated by the carboxylic acid groups of the PMAA-PTTM ligands, forming a sterically stabilizing layer that prevented nanoparticle aggregation and favored the production of monodisperse samples.

To confirm this hypothesis, the preparation process was repeated and samples were removed for TEM analysis from the solution at specific times after addition of the iron precursor and ammonia solution. Samples were withdrawn after 1, 5, 10, 40, 70, 130, and 310 min. The pH values of the samples withdrawn at these times were 11.32, 10.74, 9.87, 9.41, 9.04, 7.68, and 6.46, respectively.^[20] The decrease of pH with reaction time is attributed to the evaporation of ammonia during reaction. The samples were characterized by TEM (Figure 2a–f). The particle size and size distribution of these samples are shown in Figure S4, based on the statistical analysis of 100 nanoparticles. The particle size slightly increased from 4.4 nm to 5.0 nm with an increase of reaction time from 1 to 310 min. The particle size distribution was relatively constant over this period (1–310 min) and the standard deviation was between 0.4 and 0.6 nm. The retention of monodispersity in the size distribution is not only indicative of the short burst of nucleation at the beginning of the reaction and its separation from particle growth, but also shows the high stability of the ferrofluid formed.

The particle size and the particle size distribution were influenced by the molar ratio between the carboxylic acid groups in the polymer ligand and the iron precursors, as presented in Figure 3a–c. Figure S5 shows the particle size distribution of nanoparticles obtained from different molar ratios between carboxylic acid groups and $\text{FeCl}_3 \cdot 6\text{H}_2\text{O}$. With a molar ratio increasing from 0.7 (Figure 3c) to 3.4 (Figure 1a), the resulting nanoparticles became more uniform and the average diameter decreased from 6.1 nm to

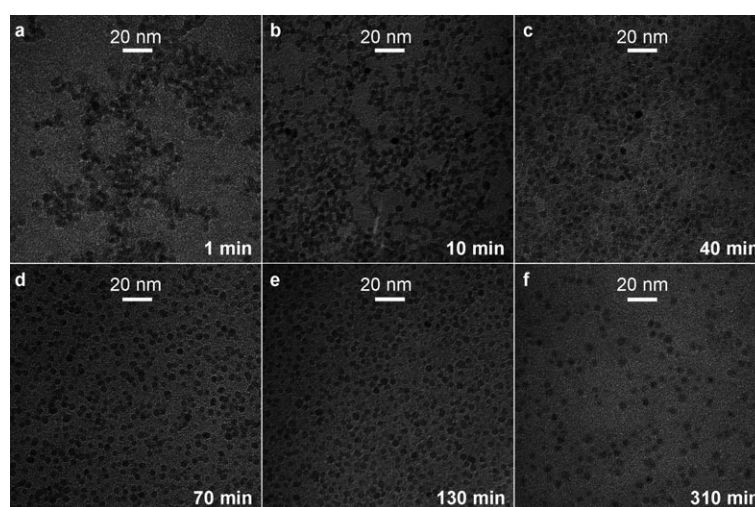


Figure 2. TEM images of PMAA-PTTM protected Fe_3O_4 nanocrystals sampled at different reaction times. The reaction times are a) 1 min, b) 10 min, c) 40 min, d) 70 min, e) 130 min, and f) 310 min.

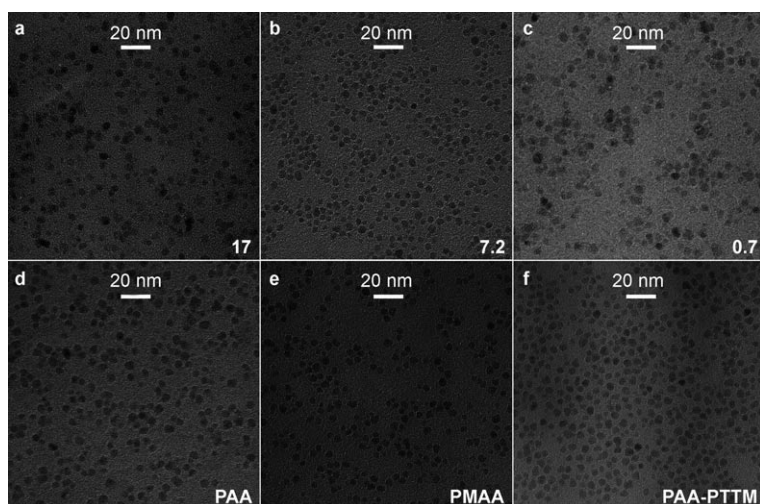


Figure 3. TEM images of Fe_3O_4 nanocrystals obtained a–c) at various molar ratios between the carboxylic acid groups in the polymer and $\text{FeCl}_3 \cdot 6\text{H}_2\text{O}$, and d–f) with different protecting polymers. The molar ratios in (a–c) are 17, 7.2, and 0.7, respectively, and the average particle sizes are 5.5 ± 0.9 nm, 4.5 ± 0.3 nm, and 6.1 ± 1.1 nm, respectively. The polymers used in (d–f) are indicated on the figures and the diameters of resulting nanocrystals are 5.6 ± 0.6 nm, 4.8 ± 0.6 nm, and 5.1 ± 0.6 nm, respectively.

4.5 nm with a decrease in standard deviation from 1.1 nm to 0.4 nm. This result indicates the role of the carboxylic acid group in the ligand in determining the particle size distribution. A further increase of the molar ratio from 3.4 to 7.2 did not have any significant effect (Figure S5). When the molar ratio was increased to 17, the particle size distribution became slightly broader. This was probably caused by the excess polymer, which increases the viscosity of the system and prevents the diffusion of reactive species. Therefore, the optimum molar ratio for producing monodisperse particles was between 3.4 and 7.2. When the molar ratio was in this range, monodisperse magnetic nanocrystals were produced with a diameter of 4.9 nm even in case of high reaction concentrations (0.1 M mixture of $\text{FeCl}_3 \cdot 6\text{H}_2\text{O}$ and $\text{FeSO}_4 \cdot 7\text{H}_2\text{O}$, which is ten times that used in the case of the synthesis of the 4.5-nm particles). Moreover, the use of $\text{FeCl}_3 \cdot 6\text{H}_2\text{O}$ and an alternative ferrous precursor such as $\text{FeCl}_2 \cdot 4\text{H}_2\text{O}$ rather than $\text{FeSO}_4 \cdot 7\text{H}_2\text{O}$ demonstrated that the shape, size, and size distribution of the resultant magnetic nanocrystals was independent of the precursors. These advantages make the present method attractive because monodisperse magnetic iron oxide nanocrystals can be prepared on a gram scale from different precursors and the production period is short.

In order to investigate further this molar ratio effect, and to investigate the influence of side and terminal groups in the ligand on particle size and size distribution, magnetic iron oxide nanoparticles were synthesized stabilized with poly(acrylic acid) (PAA, $M_n = 2000 \text{ g mol}^{-1}$), poly(methacrylic acid) (PMAA, $M_n = 35000 \text{ g mol}^{-1}$), and trithiol-terminated poly(acrylic acid) (PAA-PTTM, $M_n = 3218 \text{ g mol}^{-1}$) using the same molar ratio and reaction conditions as in the PMAA-PTTM case for synthesis of 4.5-nm particles. The TEM images of the resulting particles are shown in Figure 3d–f and the histograms of particle size distributions are

presented in Figure S5. In comparison with Figure 1a, these magnetic nanocrystals show very similar particle sizes and size distributions. The average particle sizes were between 4.8 nm and 5.6 nm, and the standard deviations were relatively constant (0.6 nm). In the case of PAA, the average particle size was slightly larger (5.6 nm). These results indicate that the carboxylic groups on the polymer chains played a dominant role in determining the particle size and size distribution compared to the side and terminal groups.

The crystalline nature of the PMAA-PTTM protected iron oxide nanoparticles was determined by X-ray powder

diffraction (XRD). Figure 4a shows the XRD patterns of 4.5-nm and 8.5-nm nanocrystals. The positions and relative intensities of all diffraction peaks match well with those expected for Fe_3O_4 rather than for $\gamma\text{-Fe}_2\text{O}_3$ (black stick and Table S1). The lattice parameters (a , derived by Rietveld refinement) for 4.5- and 8.5-nm particles are $8.350 \pm 0.001 \text{ \AA}$ and $8.366 \pm 0.001 \text{ \AA}$, respectively, which are higher than that of $\gamma\text{-Fe}_2\text{O}_3$ (JCPDS: 00-39-1346, $a = 8.346 \text{ \AA}$), and lower than that of Fe_3O_4 (JCPDS: 01-088-0315, $a = 8.375 \text{ \AA}$). The size dependence of lattice parameters is assigned to the deviation of Fe_3O_4 from stoichiometry caused by partial oxidation of the small particles.^[24] For 4.5-nm particles, the average particle size calculated by the Scherrer formula is 4.6 nm, which is almost equal to that found from the TEM studies. This result also confirms the high crystallinity and monodispersity of the nanoparticles. For 8.5-nm particles, the calculated size is 7.4 nm, which is smaller than found from the TEM data. This discrepancy maybe caused by the broader size distribution producing a difference between the number-averaged (TEM) and volume-averaged (XRD) particle sizes. XRD is relatively insensitive to the difference between magnetite (Fe_3O_4) and maghemite ($\gamma\text{-Fe}_2\text{O}_3$), and the Raman spectrum has been proved to be an alternative tool.^[8,25] Figure 4b presents the Raman spectra of 4.5-nm magnetic iron oxide particles and the oxidized product obtained by treating 4.5-nm particles at 200°C for 2 h in oxygen atmosphere. The spectrum of the 4.5-nm particles shows the characteristic peak of magnetite at 662 cm^{-1} ,^[25] while in the Raman spectrum of the corresponding oxidized product, the intensity of this peak decreases and the characteristic peaks of maghemite are observed at 384, 471, 587 cm^{-1} .^[25] The strong peaks at 213 and 275 cm^{-1} are attributed to the stable hematite formed from maghemite.^[7,25] The nanoparticles were further characterized with Fourier transform infrared spectroscopy (FTIR).^[7,26] Figure S6 clear-

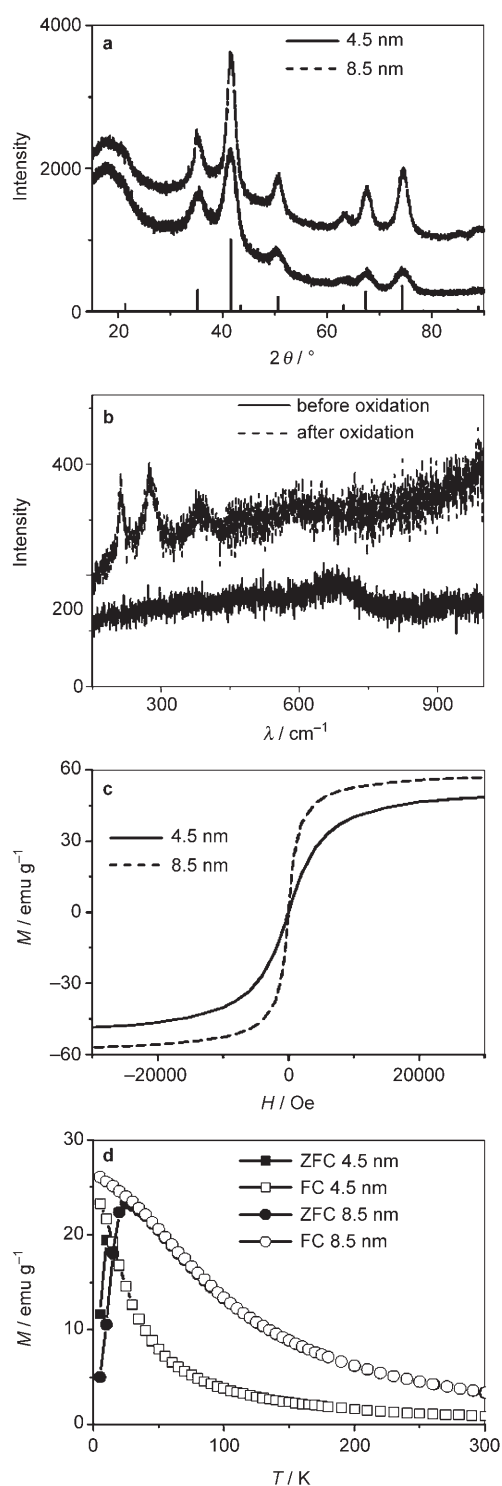


Figure 4. a) XRD patterns of 4.5-nm and 8.5-nm Fe₃O₄ nanocrystals. The lines mark the expected reflection positions for Fe₃O₄. b) Raman spectra of 4.5-nm Fe₃O₄ nanocrystals and the corresponding oxidation product. c) 300 K magnetization isotherms of 4.5-nm and 8.5-nm Fe₃O₄ particles. d) Temperature dependence of the magnetization of 4.5-nm and 8.5-nm particles measured in a 100 Oe field.

ly shows the characteristic lattice vibration of magnetite at 592 cm⁻¹.^[7] These results are consistent with the as-synthesized nanocrystals mainly being Fe₃O₄ rather than γ -Fe₂O₃.

Figure 4c shows the M - H isotherms of 4.5-nm and 8.5-nm Fe₃O₄ nanocrystals measured at 300 K; both exhibit superparamagnetic characteristics and their saturation magnetizations are 48 and 57 emu g⁻¹ Fe₃O₄, respectively. These values have been corrected for the contribution from the organic layer. Thermal gravimetric analysis (TGA, Figure S7)^[20] showed the polymer percentage of the 4.5-nm sample is 63% and the content of Fe₃O₄ is 37%. Thus the saturation magnetization of 4.5-nm Fe₃O₄ was calculated by dividing the original saturation magnetization (17.76 emu g⁻¹) by 0.37. The saturation magnetization of 8.5-nm Fe₃O₄ was calculated in the same way. For 4.5-nm Fe₃O₄, this value is higher than that of similar sized Fe₃O₄ nanoparticles ($D < 5.0$ nm; magnetic saturation, $M_s < 15$ emu g⁻¹) prepared by the standard coprecipitation method, and remains higher than such nanoparticles after annealing treatments ($D = 4.5$ nm; $M_s = 20.2$ emu g⁻¹)^[27] or oxidation into γ -Fe₂O₃ ($D = 4.0 \pm 1.0$ nm; $M_s = 40.3$ emu g⁻¹).^[28] For 8.5-nm Fe₃O₄, this value is slightly lower than that of 8.8-nm Fe₃O₄ particles with a standard deviation of 2.7 nm ($M_s = 54$ –79 emu g⁻¹).^[29] Apart from the particle size and crystallinity, there are many factors such as surface spin-canting, surface disorder, surface ligands, cation site distribution, and stoichiometry deviation that affect the magnetic properties of nanoparticles, even when synthesized by the same approach.^[28] The saturation magnetization difference between the present and previously reported materials can be assigned to these effects. According to the Langevin equation, the magnetic particle diameter (D) can be calculated from Equation 1,

$$D = \left(\frac{18kT}{\pi M_s} \sqrt{\frac{\chi_i}{3m_s H_0}} \right)^{1/3} \quad (1)$$

where k is the Boltzmann constant and T is the absolute temperature. M_s and m_s are the saturation magnetization of bulk Fe₃O₄ and nanosized Fe₃O₄, respectively. χ_i is the initial susceptibility calculated in the low-field region where the M - H relationship is linear. $1/H_0$ is obtained by extrapolating M to 0 at high field where the relationship between M and $1/H$ is linear.^[28] The calculated sizes of the as-synthesized Fe₃O₄ materials are 4.6 and 7.2 nm, respectively. For the smaller particles, the calculated size is in agreement with that obtained from TEM and XRD data. For the large particles, the calculated size is slightly smaller than the TEM and the XRD results. This discrepancy can be explained by interparticle interactions and the broader particle size distribution in the case of the larger particles because these factors determine the derivation of the Langevin function used to describe the magnetization curve.^[28]

Figure 4d presents the temperature dependence of the magnetization measured with zero-field cooling (ZFC) and field cooling (FC) procedures in an applied magnetic field of 100 Oe for $5 \text{ K} \leq T \leq 300 \text{ K}$. The divergence point of ZFC and FC curves is defined as the blocking temperature (T_b). The correlation between T_b and the volume of the nanocrystals is consistent with the Stoner–Wohlfarth theory, in which

magnetocrystalline anisotropy energy (E_a) is proportional to the volume and the anisotropy constant (K_{an}).^[30] Therefore, the larger volume nanocrystals have a high anisotropy energy and a higher blocking temperature. When E_a becomes comparable with the thermal energy (kT , where k is the Boltzmann constant), thermal activation can overcome the anisotropy energy barrier and the nanoparticles become superparamagnetic. For 4.5-nm Fe_3O_4 nanocrystals, ZFC and FC curves clearly show divergence at the blocking temperature of 25 K. Above the blocking temperature, the magnetization decreases sharply and presents superparamagnetic behavior. This sharp change not only reflects the size-dependent magnetic property, but also indicates the particle size distribution. The 8.5-nm Fe_3O_4 nanocrystals display a higher blocking temperature of 95 K and a less pronounced decrease of the magnetization with increasing temperature owing to the larger particle size and the broader size distribution than the 4.5-nm particles. Fe_3O_4 nanocrystals with a similar mean size but a broader size distribution (4.9 ± 1.4 nm) also display a less pronounced decrease of the magnetization above the blocking temperature (Figure S2).^[20] In addition, the blocking temperature (85 K) of the sample with the broader size distribution is much higher than that of the 4.5-nm Fe_3O_4 because there are of the order of 22% “larger” particles ($D > 6.0$ nm) in the sample. This result indicates that the particle size distribution has an important effect on the measured blocking temperature, which is sensitive to the presence of even a small percentage of larger particles. The sharp variation of T_b is similar to that found for other oxide nanoparticles such as CoO, MnO, and NiO.^[31,32] For example, T_b of NiO nanoparticles increases from 10 to 15 K with increase of particle size from 3 to 7 nm.^[32] For superparamagnetic nanocrystals, the relationship between blocking temperature (T_b) and particle volume (V) can be expressed as

$$K_{an}V = 25kT_b \quad (2)$$

where K_{an} is the anisotropy constant and k is the Boltzmann constant.^[33] Based on the blocking temperatures of the 4.5-nm and 8.5-nm Fe_3O_4 samples, their anisotropy constant values are estimated to be 1.81×10^5 and $1.02 \times 10^5 \text{ J m}^{-3}$, respectively, which are close to previously reported values for Fe_3O_4 nanoparticles.^[33]

The water solubility and colloidal stability of magnetic iron oxide nanoparticles are very important for biological applications. In the case of magnetic iron oxide nanoparticles (Fe_3O_4 and $\gamma\text{-Fe}_2\text{O}_3$) prepared from aqueous solutions in the absence of a stabilizer, dried particle powders cannot usually be redispersed in neutral water and thus the samples are stored as an aqueous fluid whose stability is strongly dependent on the pH and ionic strength.^[34] Dried powders of the present samples were easily redispersed in neutral water solutions and their hydrodynamic sizes were determined by dynamic light scattering (DLS) to be 8.7 and 11.7 nm (Figure S8), for the 4.5-nm (directly synthesized) and seed-grown particles, respectively.^[20] Their narrow FWHMs (full width at half maximum, 5.4 nm and 9.4 nm) further demon-

strate the monodispersity of the nanoparticles. For the 4.5-nm-diameter sample, DLS measurements showed that solutions with concentrations up to 20 mg mL^{-1} were stable over a wide pH range of 3.5 to 12 (Figure S9).^[20] Although the average hydrodynamic diameter of the nanoparticles did not change with increase of pH, the size distribution changed slightly. This is probably caused by conformational changes in the polymer chain.^[35] The conformational change of poly(methacrylic acid) is not a homogenous ionization with increasing pH: increasing pH leads to the ionization of a number of carboxylic acid groups, and produces a coiled hydrophobic part surrounded by an ionized corona.^[35] The ratio of hydrophobic to hydrophilic segments determines the polymer extension and the hydrodynamic diameter of the nanoparticles.

The excellent water-solubility of the particles is attributed to the free carboxylic acid groups of the stabilizing PMAA-PTTM ligand that is bound to the particle surface, that is, not all the carboxylic acid groups in the ligand are bound to the iron species on the particle surfaces. Figure S6 shows the FTIR spectra of pure polymer and 4.5-nm particles protected with polymer ligand.^[20] Compared to the spectrum of pure PMAA-PTTM, the spectrum of the nanoparticles shows the characteristic peaks of the carboxylic group at 3124 cm^{-1} (-OH) and 1704 cm^{-1} (-CO-), and the thiol group at 2360 cm^{-1} . In contrast, the asymmetric and symmetric stretching bands of carboxylate (-COO-) are shifted from $1485, 1390 \text{ cm}^{-1}$ to 1556 and 1402 cm^{-1} , respectively. The difference, Δ , between the asymmetric and symmetric bands increases from 95 to 154 cm^{-1} . It is known that the carboxylate ion may coordinate via unidentate, bidentate, or bridging modes that may be distinguished according to Δ .^[36] The present case, $\Delta = 154 \text{ cm}^{-1}$, indicates unidentate carboxylate coordination to Fe. The particles also have been characterized by TGA (Figure S7).^[20] The TGA of 4.5-nm Fe_3O_4 showed two decomposition stages as found for free PMAA-PTTM; however, these two onset decomposition temperatures occurred about 20°C and 60°C higher. This is possibly because of heat-capacity differences between the nanoparticles and the pure polymer or due to stabilization of the polymer upon binding to the nanoparticles. The weight loss at the first stage in both curves was approximately 10%, which is close to the terminal thiol group mass percentage (10.7 w/w%) in the polymer. This result suggests that the polymer decomposition begins at the terminal group and supports the existence of free thiol groups. The main weight loss occurred in the second stage and is attributed to the decomposition of the side group and the polymer backbone. The polymer percentage on the 4.5-nm Fe_3O_4 surface was about 63 w/w%. Assuming that the density of Fe_3O_4 nanoparticles is equal to that of the bulk phase (4.8 g cm^{-3}) and that the nanoparticles are spherical in shape, there are thus an average of approximately 50 polymer molecules associated with each particle.

These two different reactive functional groups (i.e., carboxylic acids and thiols) carried by the ligands provide a number of choices for conjugation reactions of the polymer-protected nanoparticles. For example, thiol groups can react with a hetero-bifunctional crosslinker such as *N*-succinimidyl-

3-(2-pyridylthio)propionate (SPDP) and sulfosuccinimidyl 4-(*N*-maleimidomethyl)cyclohexane-1-carboxylate (Sulfo-SMCC) to introduce reactive functionalities for further conjugation,^[2,3] while the carboxylic groups can maintain good water-solubility for the nanoparticles. We have developed another conjugation method for the thiol group to yield strongly fluorescent magnetic nanocrystals (Scheme 1). Glutamic acid and *O*-phthalaldehyde were chosen for conjugation to afford Fe_3O_4 nanocrystals functionalized with isoindole, referred to as $\text{Glu-Fe}_3\text{O}_4$. These $\text{Glu-Fe}_3\text{O}_4$ particles were then used for further conjugation of the free carboxylic acid groups using rhodamine 110 (R110). The reaction was catalyzed by 1-[3-(dimethylaminopropyl)-3-ethylcarbodiimidehydrochloride (EDC) and *N*-hydroxysulfosuccinimide sodium salt (NHS),^[37] and afforded $\text{Glu-Fe}_3\text{O}_4$ -R110 particles.

Figure 5a shows photographs of solutions of Fe_3O_4 nanoparticles, and the conjugated $\text{Glu-Fe}_3\text{O}_4$ and $\text{Glu-Fe}_3\text{O}_4$ -R110 nanoparticles before and after being irradiated with 365-nm UV light. It can be seen that the parent Fe_3O_4 nanoparticle solution does not show any fluorescence. After reaction with glutamic acid in the presence of *O*-phthalaldehyde to form $\text{Glu-Fe}_3\text{O}_4$, the solution shows strong blue fluorescence that derives from the 1-alkylthio-2-alkyl-substituted isoindole (Scheme 1).^[38] The maximum emission peak of the isoindole-conjugated nanoparticles at 421 nm is shown in Figure 5b (solid line). In the corresponding excitation spectrum (dashed line), two peaks are observed at 370 and 385 nm. There is little difference between the UV absorbance spectra of the Fe_3O_4 nanoparticles and that of $\text{Glu-Fe}_3\text{O}_4$ (short-dash line and short-dot line) that can be attributed to the strong dominant absorbance of the Fe_3O_4 nanoparticles.

The physical mixture of 4.5 nm Fe_3O_4 nanocrystals and R110 did not show any fluorescence after dialysis (dash-dot line in Figure 5b). This shows that the free R110 was totally removed by dialysis.^[37] The $\text{Glu-Fe}_3\text{O}_4$ -R110 conjugate showed the characteristic emission peaks of 1-alkylthio-2-alkyl-substituted isoindole and R110 at 425 and 522 nm (dash-dot-dot line in Figure 5b), respectively under excitation at 385 nm. The UV absorbance showed a small absorption peak attributed to R110 at 496 nm (short-dash-dot line in Figure 5b). These results show that R110 has been successfully conjugated with $\text{Glu-Fe}_3\text{O}_4$. The maximum peak derived from 1-alkylthio-2-alkyl-substituted isoindole in the emission spectrum is red-shifted from 421 to 425 nm in comparison with $\text{Glu-Fe}_3\text{O}_4$, while the peak derived from R110 remains at the 522 nm found for the pure R110 ligand. The reason for this shift is yet unclear; it may be caused by fluorescence resonance energy transfer (FRET).^[39] The dotted line shows the excitation spectrum of $\text{Glu-Fe}_3\text{O}_4$ -R110 obtained from an excitation wavelength of 522 nm. Figure 5c shows the DLS data for Fe_3O_4 , $\text{Glu-Fe}_3\text{O}_4$, $\text{Glu-Fe}_3\text{O}_4$ -R110. It can be seen that the hydrodynamic diameter of the Fe_3O_4 nanoparticles is maintained after conjugation, which indicates the good stability of the nanoparticles and that no aggregation occurred during the conjugation reaction.

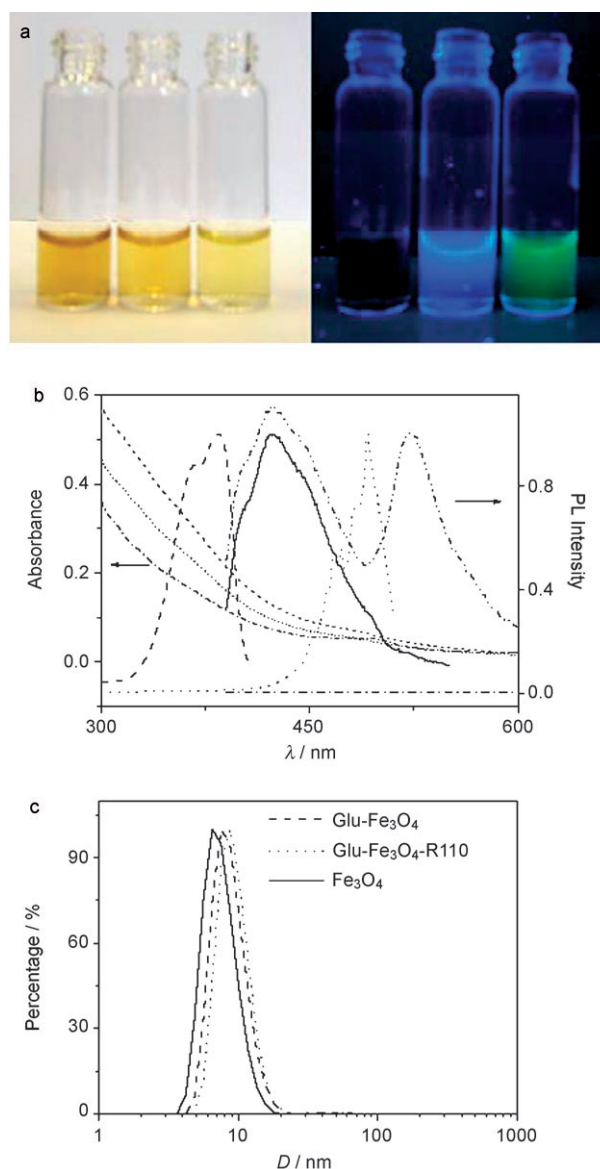


Figure 5. a) Photographs of (left to right in each picture) Fe_3O_4 nanocrystals, $\text{Glu-Fe}_3\text{O}_4$, and $\text{Glu-Fe}_3\text{O}_4$ -R110 before (left panel) and after (right panel) excitation with 365-nm UV light; b) UV absorbance and photoluminescence spectra; the solid, dashed, and short-dash lines are the emission, excitation and UV absorption spectra of $\text{Glu-Fe}_3\text{O}_4$, respectively. The short-dotted line shows the UV-absorption of the parent Fe_3O_4 solution; the dash-dot line is the emission spectrum of a physical mixture of Fe_3O_4 and R110 after dialysis for 24 h, the dash-dot-dot, short-dash-dot, and dotted lines represent the emission, UV absorption, and excitation spectra, respectively, of $\text{Glu-Fe}_3\text{O}_4$ -R110. c) Hydrodynamic diameters determined by DLS.

3. Conclusions

Fe_3O_4 nanocrystals have been prepared without any size selection processes by a coprecipitation route in the presence of thiol-terminated PMAA. The molar ratio between the carboxylic acid group and the iron precursors plays an important role in determining the particle size and the size distribution. The narrow particle size distribution is attributed to the short burst of nucleation and its separation from

subsequent growth processes. The dried nanoparticles are readily redispersed in water and the colloids are very stable over a wide pH range. Exploiting the thiol group in the ligand, blue fluorescent magnetic nanoparticles can be produced by conjugation with glutamic acid in the presence of *O*-phthalaldehyde at room temperature. The free carboxylic groups from the polymer ligand can also be used for further functionalization. Such multifunctional Fe_3O_4 nanocrystals may be used in labeling, detection, separation, and assay of molecules such as proteins, peptides, antibodies, and amino acids. The synthetic approach affords high-quality, water-soluble Fe_3O_4 nanocrystals directly with two different kinds of reactive functional groups in the ligand.

4. Experimental Section

Synthesis of 4.5-nm Fe_3O_4 particles: The polymer PMAA-PTTM^[19] aqueous solution (50 mL, 0.768 mM, pH = 4.87) was first purged with argon to remove oxygen and then heated to reflux (102°C). Next, the diluted HCl solution (1 mL, pH = 1.98) containing $\text{FeCl}_3 \cdot 6\text{H}_2\text{O}$ (0.54 mmol) and $\text{FeSO}_4 \cdot 7\text{H}_2\text{O}$ (0.27 mmol) was injected into the hot solution, followed by concentrated ammonia solution (15 mL), this took less than 3 s. Upon addition of the ammonia, the solution became black and the temperature dropped to 85°C. It took 10 min to increase the temperature to 102°C, and the solution was then kept refluxing for 2 h at this temperature. The solution was then cooled to 60°C and concentrated to 10 mL volume under a reduced pressure of 72 N m⁻². The black solution obtained was dialyzed against Milli-Q water (the molecular weight cut-off was 10000 g mol⁻¹) for 72 h to remove any free PMAA-PTTM ligand. The dialyzed solution was then evaporated under reduced pressure. The dried product was collected with a permanent magnet (0.5 T) as a black powder.

Preparation of 8.5-nm Fe_3O_4 particles by the seed-mediated growth method: PMAA-PTTM (15.3 μmol) and 4.5-nm-diameter particles (21.2 mg) were dissolved in Milli-Q H₂O (20 mL). The mixture was bubbled with argon and preheated to reflux and the diluted HCl solution (500 μL, pH = 1.98) containing $\text{FeCl}_3 \cdot 6\text{H}_2\text{O}$ (21.5 μmol) and $\text{FeSO}_4 \cdot 7\text{H}_2\text{O}$ (10.8 μmol) was injected rapidly into the hot solution, followed by the addition of concentrated ammonia solution (8 mL). After reflux for 2 h at 102°C, the solution was cooled to 60°C and a similar purification procedure was applied as used for the 4.5-nm particles.

Conjugation of Fe_3O_4 nanocrystals via thiol group: 4.5-nm Fe_3O_4 nanocrystals (5.0 mg) were dissolved in Milli-Q H₂O (5.0 mL) and the pH was adjusted to 10.7 by addition of diluted NaOH solution (1.0 M). To this particle solution, *O*-phthalaldehyde solution in methanol (700 μL, 2.0 mg mL⁻¹) was added, followed by 1 mL glutamic acid water solution (1.0 mg mL⁻¹). The reaction was carried out for 2 hours at room temperature (if heated to 50°C, the reaction occurred in less than 5 minutes) and the excess of *O*-phthalaldehyde and glutamic acid were removed by di-

alysis. The dialyzed solution was then dried and the isoin-dole-functionalized Fe_3O_4 nanocrystals (Glu- Fe_3O_4) were used for further conjugation of the carboxylic functional groups.

Conjugation of Fe_3O_4 nanocrystals via carboxylic group: Glu- Fe_3O_4 , EDC, NHS, and R110 were separately dissolved in phosphate buffered saline (PBS) solution (1 mL, pH = 7.0). The concentration of R110 was 0.1 mg mL⁻¹ and 1.0 mg mL⁻¹ for the other reagents. EDC (145 μL) and NHS (40 μL) were sequentially added to Glu- Fe_3O_4 solution (1 mL) and then R110 (280 μL) was added and the mixture was stirred for 4 h at room temperature. The resulting conjugate (Glu- Fe_3O_4 -R110) was purified by dialysis for 24 h. As a comparison, a mixture of 4.5-nm Fe_3O_4 and R110 with the same molar ratio was also dialyzed for 24 h.

Characterization: Low-resolution TEM images were collected on a JEOL-2000FX electron microscope operating at an accelerating voltage of 200 kV. High-resolution TEM data were collected on a JEOL-2011 electron microscope operating at an accelerating voltage of 200 kV. Images were recorded with a Gatan 794 CCD camera. XRD data were collected on a Panalytical X'pert Pro Multi-Purpose X-ray diffractometer with Co Kα1 radiation ($\lambda = 1.78901 \text{ \AA}$). Raman spectra were measured on a HR JOBIN YVON spectrometer using a laser wavelength of 632 nm and a 25% filter. Magnetic properties were recorded on a Quantum Design MPMS SQUID magnetometer. The UV absorbance data were collected on a Northstar Scientific UV Spectrometer by using a 96-well plate as sample holder. Photoluminescence spectra were measured on SIM AMINCO spectrometer with a 150 μL sample. DLS measurements were performed on a ZETASIZER Nano-Series instrument.

Acknowledgements

We thank the EPSRC (EP/C511794/1) for funding and the Royal Society for a Royal Society Research Fellowship (to A.I.C.) and Wolfson Merit Award (to M.J.R.). We thank Dr. A. D. Bates (School of Biological Sciences, University of Liverpool) for access to the fluorescence spectrometer and the Centre for Materials Discovery for access to facilities.

- [1] H. W. Gu, K. M. Xu, C. J. Xu, B. Xu, *Chem. Commun.* **2006**, 941–949.
- [2] M. Lewin, N. Carlesso, C. H. Tung, X. W. Tang, D. Cory, D. T. Scadden, R. Weissleder, *Nat. Biotechnol.* **2000**, 18, 410–414.
- [3] Y. M. Huh, Y. W. Jun, H. T. Song, S. Kim, J. S. Choi, J. H. Lee, S. Yoon, K. S. Kim, J. S. Shin, J. S. Suh, J. Cheon, *J. Am. Chem. Soc.* **2005**, 127, 12387–12391.
- [4] V. P. Torchilin, *Eur. J. Pharm. Sci.* **2000**, 11, S81–S91.
- [5] A. Jordan, R. Scholz, K. Maier-Hauff, M. Johannsen, P. Wust, J. Nadobny, H. Schirra, H. Schmidt, S. Deger, S. Loening, W. Lanksch, R. Felix, *J. Magn. Magn. Mater.* **2001**, 225, 118–126.
- [6] B. L. Cushing, V. L. Kolesnichenko, C. J. O'Connor, *Chem. Rev.* **2004**, 104, 3893–3946.

- [7] U. Schwertmann, R. Cornell, *Iron Oxides in the Laboratory - Preparation and Characterization*, 2nd ed., Wiley-VCH, Weinheim, **2000**, pp. 5–28.
- [8] M. F. Casula, Y. W. Jun, D. J. Zaziski, E. M. Chan, A. Corrias, A. P. Alivisatos, *J. Am. Chem. Soc.* **2006**, *128*, 1675–1682.
- [9] S. H. Sun, H. Zeng, *J. Am. Chem. Soc.* **2002**, *124*, 8204–8205.
- [10] J. Park, E. Lee, N. M. Hwang, M. S. Kang, S. C. Kim, Y. Hwang, J. G. Park, H. J. Noh, J. Y. Kini, J. H. Park, T. Hyeon, *Angew. Chem. Int. Ed.* **2005**, *44*, 2872–2877; *Angew. Chem.* **2005**, *117*, 2932–2937.
- [11] A. B. Bourlinos, A. Bakandritsos, V. Georgakilas, D. Petridis, *Chem. Mater.* **2002**, *14*, 3226–3228.
- [12] Z. Li, H. Chen, H. B. Bao, M. Y. Gao, *Chem. Mater.* **2004**, *16*, 1391–1393.
- [13] Z. Li, Q. Sun, M. Y. Gao, *Angew. Chem. Int. Ed.* **2005**, *44*, 123–126; *Angew. Chem.* **2005**, *117*, 125–128.
- [14] Z. Li, L. Wei, M. Y. Gao, H. Lei, *Adv. Mater.* **2005**, *17*, 1001–1005.
- [15] F. Q. Hu, L. Wei, Z. Zhou, Y. L. Ran, Z. Li, M. Y. Gao, *Adv. Mater.* **2006**, *18*, 2553–2556.
- [16] F. Q. Hu, Z. Li, C. F. Tu, M. Y. Gao, *J. Colloid Interface Sci.* **2007**, *311*, 469–474.
- [17] R. Weissleder, K. Kelly, E. Y. Sun, T. Shtatland, L. Josephson, *Nat. Biotechnol.* **2005**, *23*, 1418–1423.
- [18] I. Hussain, S. Graham, Z. X. Wang, B. Tan, D. C. Sherrington, S. P. Rannard, A. I. Cooper, M. Brust, *J. Am. Chem. Soc.* **2005**, *127*, 16398–16399.
- [19] Z. Wang, B. Tan, I. Hussain, N. Schaeffer, M. F. Wyatt, M. Brust, A. I. Cooper, *Langmuir* **2007**, *23*, 885–895.
- [20] See Supporting Information for details.
- [21] C. B. Murray, D. J. Norris, M. G. Bawendi, *J. Am. Chem. Soc.* **1993**, *115*, 8706–8715.
- [22] Y. Yin, A. P. Alivisatos, *Nature* **2005**, *437*, 664–670.
- [23] M. Mikhaylova, D. K. Kim, N. Bobrysheva, M. Osmolowsky, V. Semenov, T. Tsakalakos, M. Muhammed, *Langmuir* **2004**, *20*, 2472–2477.
- [24] T. J. Daou, G. Pourroy, S. Begin-Colin, J. M. Greneche, C. Ulhaq-Bouillet, P. Legare, P. Bernhardt, C. Leuvrey, G. Rogez, *Chem. Mater.* **2006**, *18*, 4399–4404.
- [25] D. L. A. de Faria, S. V. Silva, M. T. de Oliveira, *J. Raman Spectrosc.* **1997**, *28*, 873–878.
- [26] P. Tartaj, M. D. Morales, S. Veintemillas-Verdaguer, T. Gonzalez-Carreno, C. J. Serna, *J. Phys. D-Appl. Phys.* **2003**, *36*, R182–R197.
- [27] J. H. Wu, S. P. Ko, H. L. Liu, S. Kim, J. S. Ju, Y. Keun-Kim, *Mater. Lett.* **2007**, *61*, 3124–3129.
- [28] M. P. Morales, S. Veintemillas-Verdaguer, M. I. Montero, C. J. Serna, A. Roig, L. Casas, B. Martinez, F. Sandiumenge, *Chem. Mater.* **1999**, *11*, 3058–3064.
- [29] L. A. Harris, J. D. Goff, A. Y. Carmichael, J. S. Riffle, J. J. Harburn, T. G. St Pierre, M. Saunders, *Chem. Mater.* **2003**, *15*, 1367–1377.
- [30] C. Liu, B. S. Zou, A. J. Rondinone, J. Zhang, *J. Am. Chem. Soc.* **2000**, *122*, 6263–6267.
- [31] M. Ghosh, E. V. Sampathkumaran, C. N. R. Rao, *Chem. Mater.* **2005**, *17*, 2348–2352.
- [32] M. Ghosh, K. Biswas, A. Sundaresan, C. N. R. Rao, *J. Mater. Chem.* **2006**, *16*, 106–111.
- [33] L. Balcells, O. Iglesias, A. Labarta, *Phys. Rev. B: Condens. Matter Mater. Phys.* **1997**, *55*, 8940–8944.
- [34] Y. S. Kang, S. Risbud, J. F. Rabolt, P. Stroeve, *Chem. Mater.* **1996**, *8*, 2209–2211.
- [35] A. F. Olea, J. K. Thomas, *Macromolecules* **1989**, *22*, 1165–1169.
- [36] K. Nakamoto, *Infrared and Raman Spectra of Inorganic and Coordination Compounds*, 5th ed., Wiley Interscience, New York **1997**, pp. 59–62.
- [37] Y. Sahoo, A. Goodarzi, M. T. Swihart, T. Y. Ohulchanskyy, N. Kaur, E. P. Furlani, P. N. Prasad, *J. Phys. Chem. B* **2005**, *109*, 3879–3885.
- [38] S. S. Simons, D. F. Johnson, *J. Am. Chem. Soc.* **1976**, *98*, 7098–7099.
- [39] T. Förster, *Ann. Phys.* **1948**, *2*, 55–57.

Received: July 23, 2007

Published online on January 22, 2008